# The CLAS12 Forward Electromagnetic Calorimeter

G. Asryan[f], Sh. Chandavar[c], T. Chetry[c], N. Compton[c], A. Daniel[c], N. Dashyan[f], N. Gevorgyan[f], Y. Ghandilyan[f], K. Giovanetti[g], K. Griffioen[b], K. Hicks[c], D. Kashy[a], G. Khachatryan[f], M. Khandaker[d], J. Riso[b], A. Simonyan[f], C. Salgado[d], C. Smith[e], S. Stepanyan[a], W. Tang[c], H. Voskanyan[f], M. Yurov[h]

[a]*Thomas Jefferson National Accelerator Facility, Newport News, VA 23606, USA*
[b]*The College of William and Mary, Williamsburg, VA 23185, USA*
[c]*Ohio University, Athens, OH 45701, USA*
[d]*Norfolk State University, Norfolk, VA 23504, USA*
[e]*University of Virginia, Charlottesville, VA 22901, USA*
[f]*A. Alikhanyan National Science Laboratory, Yerevan, 375036, Armenia*
[g]*James Madison University, Harrisonburg, VA 22807 , USA*
[h]*Kyungpook National University, Daegu 41566, Republic of Korea*

**Abstract**

The CLAS12 Forward Detector includes six independent lead-scintillator electromagnetic sampling calorimeters to provide the primary electron trigger and extend the CLAS12 detection capability to photons and neutrons. Each calorimeter package consists of two modules, the legacy Electromagnetic Calorimeter (EC) previously used in the CLAS detector, and a new pre-shower calorimeter (PCAL) located in front of the EC to extend the total detector radiation length, in order to fully absorb the electromagnetic showers induced by electrons with energies up to 12 GeV. Both calorimeters use a novel triangular hodoscope geometry with stereo readout. The PCAL uses an upgraded design to provide the high spatial resolution necessary for reconstructing $\pi^0$ and $\eta$ decays, and neutrons with high efficiency. This paper treats the design, construction, and calibration of the PCAL and the preliminary combined performance of both detectors.

PACS:29.40.Vj
Keywords: CLAS12, sampling calorimeter, plastic scintillator, particle identification

## 1. Overview

A primary goal of the CLAS12 physics program [1] is to provide a systematic study of the internal dynamics of the nucleon by accessing the nucleon's Generalized Parton Distributions (GPDs). This is accomplished through measurements of deeply virtual Compton scattering (DVCS), deeply virtual meson production (DVMP), and single spin asymmetries (SSA). These experiments require accurate kinematical analysis of neutral and charged particles at high momentum. In particular, all CLAS12 electroproduction experiments require the efficient detection and reliable identification of energetic electrons, photons, and neutrons using the forward electromagnetic calorimeter (ECAL).

For CLAS12 [2] it was necessary to augment the existing CLAS calorimeter (EC) [3] with a separate pre-shower calorimeter (PCAL) installed in front of the EC on the Forward Detector. Simulations using the Geant3 package showed that the thickness of the EC alone (16 radiation lengths) would not be sufficient to absorb the full energy of electromagnetic showers produced by electrons and photons with momenta above 5 GeV. Since the ECAL is used in the trigger this would ultimately reduce the efficiency for detection of the highest energy electrons. High energy neutral mesons ($\pi^0$,$\eta$) present a challenge as well. Neutral mesons decay immediately into two photons with an opening angle that decreases as the momentum increases. This calls for an improved calorimeter position resolution in order to resolve the two decay photons in the full momentum range of interest up to few GeV. This is particularly critical for the reconstruction of the DVCS final state, since a single high energy photon is produced in the reaction $ep \to e'p'\gamma$ and the largest background to this process is from single $\pi^0$ production, $ep \to e'p'\pi^0$. In addition, direct $\pi^0$ production complements the DVCS measurements by accessing GPDs at low and high momentum transfer $|t|$. Clearly, accurate and efficient $\pi^0$ reconstruction is crucial to separate these two processes. Finally, the capability to detect and identify neutral mesons from the two-photons decay is of particular importance for the CLAS12 meson spectroscopy program, since these states are part of many of the reactions of interest [4].

The performance requirements of the PCAL were therefore driven by two factors: 1) electromagnetic shower containment within the ECAL volume for the highest CLAS12 electron energies to preserve the desired energy resolution and efficiency and 2) improved spatial resolution to cleanly separate multiple shower clusters.

## 2. Requirements

The physics requirements for the ECAL are similar to those outlined for the CLAS 6 GeV program [3]. For CLAS12 the

performance goals reflect operation at twice the CLAS program beam energy:

- $e/\gamma$ energy resolution $\sigma/E \leq 0.1/\sqrt{E(\mathrm{GeV})}$;
- Position resolution $\delta r \approx 1$ cm for showers;
- $\pi/e$ rejection greater than 99% at $E \geq 5$ GeV;
- Mass resolution for $\pi^0 \rightarrow 2\gamma$ decays $\delta m/m \leq 0.1$;
- Neutron detection efficiency > 50% for $E_n > 1$ GeV;
- Time-of-flight resolution ≈0.5 ns.

A sampling calorimeter with high spatial resolution would normally employ a tower/matrix-like structure of independent readout modules such as used in collider experiments. The choice of a hodoscope design for CLAS was determined by two factors: 1) reduced cost of instrumenting a large surface area (50 m$^2$) and 2) the need for uniformity of response due to the calorimeter defining the cross section normalization [5].

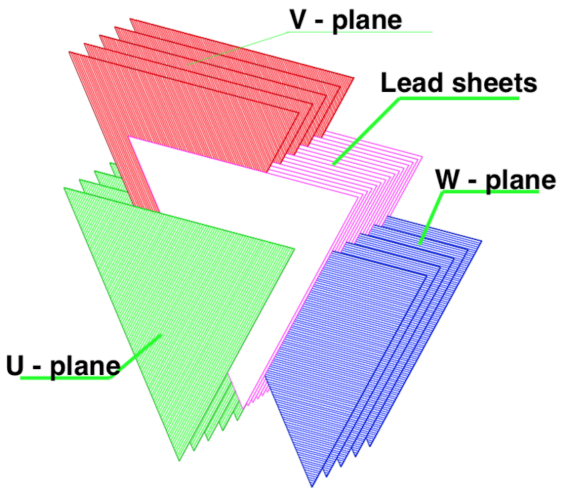


Figure 1: Schematic view showing the interleaving of scintillator layers with lead sheets. For PCAL there are five layers of scintillator strips that define each of the U, V, and W planes.

To accommodate the hexagonal geometry of CLAS and CLAS12, both the EC and PCAL use a triangular hodoscope layout. The scintillator layers have three alternating stereo readout planes named U, V, and W, which are interleaved with layers of lead as illustrated in Fig. 1. The readout planes are divided into scintillator strips of varying lengths but with a fixed cross-sectional area. In each stereo readout layer the strips are oriented parallel to one of the sides of the triangle. For the U-view, the strips are parallel to the base of the triangle, farthest from the beamline. For the W-view, the strips are parallel to the U photomultiplier tube (PMT) readout side. For the V view, the strips are parallel to the last remaining side. The light output from each scintillator belonging to a layer is optically summed and read out by a PMT.

The design parameters of the PCAL were originally established using Geant3 simulations of the PCAL-EC system (together referred to as the ECAL). These studies are described in detail in Ref. [6] and summarized below. The mechanical design depends on the number of scintillator-lead layers, on the angular coverage of the PCAL, and on the degree of readout segmentation. These parameters were determined by the physics requirements for the detection and identification of high energy electrons, photons, and $\pi^0$ mesons via $2\gamma$ decay.

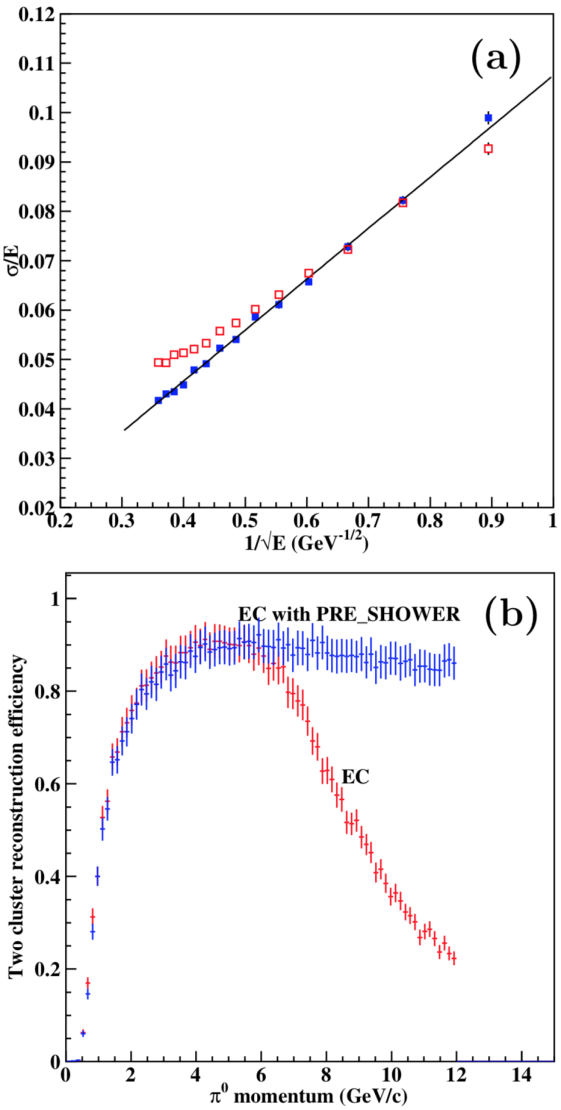


Figure 2: Comparison of simulated performance of the combined PCAL+EC calorimeter (blue points) and EC only (red points) at CLAS12 energies. a) Energy resolution as a function of inverse square root of energy. b) Reconstruction efficiency of two clusters from $\pi^0$ decay photons as a function of pion momentum.

Initial simulations were carried out with 15 layers of lead and scintillator (similar to the inner part of the EC), using 3.5-cm-wide segmentation for the scintillator layers, corresponding to about 108 readout channels in each stereo view. For comparison the EC uses 10-cm-wide strips. Events were generated using a uniform distribution of $\pi^0 \rightarrow 2\gamma$ decays at the target with meson momenta up to 12 GeV. Showers were identified using the standard cluster reconstruction algorithm of the EC [7], but applied to both the PCAL and EC. As shown in Fig. 2, the

combined PCAL and EC system retains good energy resolution, $\sigma/E \approx 0.1 \times E^{-1/2}$, with constant efficiency for two cluster reconstruction up to the highest momenta.

Additional simulations were performed using variable segmentation of the scintillator layers. Keeping constant the total number of readout channels per sector, it was found that the maximum efficiency can be obtained if half of each stereo layer is equipped with 4.5 cm strips and half with 9.0 cm strips (double strip readout). The triangular stereo layers overlap such that there is always a region with 4.5 cm strips in one of the stereo layers, as shown in Fig. 3. There is only a small loss of two-cluster efficiency at the highest momenta for this geometry compared with 4.5 cm strips in all stereo layers. It should be noted that at forward angles (short U-strips) where most of the high energy $\pi^0$ are produced, all three stereo readout views have the high-density readout segmentation needed to resolve the small $2\gamma$ opening angles of $< 3°$.

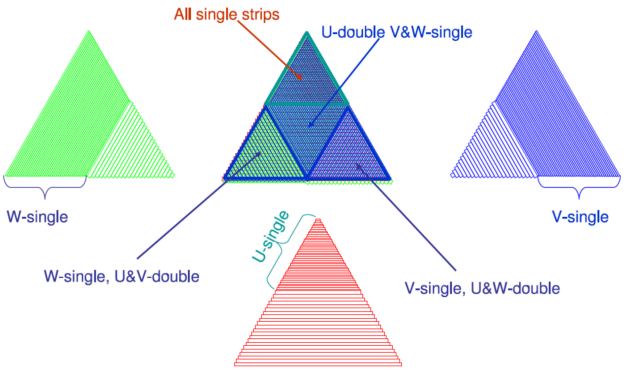


Figure 3: Segmentation pattern for different PCAL stereo readout planes (U, V, and W). There is always a region with single width (4.5 cm) readout segmentation in one of the stereo layers. The U PMTs are read out from the left side of the triangle, as seen in this view from the target, while the V and W strips are read out from PMTs installed along the base of the triangle.

## 3. Design

The PCAL geometry [8] is shown schematically in Fig. 4. The active area of the PCAL is an isosceles triangle with a base length of 394 cm and a base angle $\alpha = 62.9°$. The apex of the triangle is nearest the beamline, while a line from the CLAS12 target center to the front face of each module subtends an angle of 25° with respect to the beamline. The nominal length of this line to the first scintillator plane is 697.8 cm. Each PCAL module is composed of 15 layers of 1-cm-thick scintillator sandwiched with 14 layers of 0.22-cm-thick lead, similar to the inner calorimeter of the CLAS EC [3]. Light generated in the scintillator strips by ionizing radiation is down-converted using wavelength-shifting (WLS) fibers inserted inside holes running the length of the strips (see Fig. 5). The fibers also transport the light to PMT housing adapters located along the base and U readout side of the triangle. Each scintillator and lead layer is separated by a 50 $\mu$m Teflon sheet and the entire scintillator/lead volume is confined within a triangular shaped box. Note the EC uses a projective geometry where each scintillator layer subtends the same solid angle as seen from the target, whereas the PCAL does not. The PCAL active area is slightly larger than the acceptance of the EC, as indicated in Fig. 4 by projecting the EC toward the target through the location of the last layer of the PCAL.

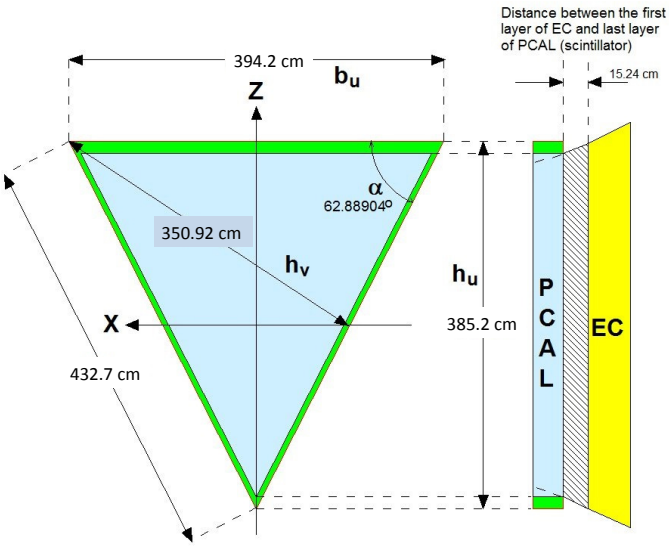


Figure 4: A schematic view showing the dimensions of a PCAL module. The length of the longest U scintillator strip at the base of the triangle is 394.2 cm and 432.7 cm for the V and W strips along the sides of the triangle.

There are 84 strips in each U-view layer, and 77 strips in each of the V and W layers, for a total of 1190 scintillator strips installed in each of the six PCAL modules. Each scintillator has four WLS fibers for a total of 4760 installed and routed fibers per module. In order to optimize the number of readout channels, each pair of strips at large scattering angles are combined into a single readout channel (fibers from two adjacent strips are routed to a single PMT). For the first 52 shortest strips in U and for the last 46 longest strips in the V and W stereo readout planes the 4.5 cm (single strip) segmentation is used. For the remaining strips, 9.0-cm-wide (double strip) segmentation is used. Thus there are a total of 68 PMT readout channels for U, and 62 for V and W.

## 4. Hardware Components

A design goal for the PCAL upgrade of the ECAL was an improvement in both light yield and spatial resolution within a more limited budget. Compared to the early 1990s when the EC was designed, the lower price of wavelength shifting (WLS) fibers, combined with new techniques for the production of high light yield extruded scintillator, has enabled this cost savings. Use of embedded WLS fibers bypasses the need for costly low attenuation length scintillator (such as BC-412 used in the EC), while the readout simplification enables further improvement in light yield.

Several studies were performed [9, 10, 11] to select the optimal combination of light readout components (scintillator, WLS fiber, and PMT) needed to maximize the light yield. Based on the results of measurements and the available price

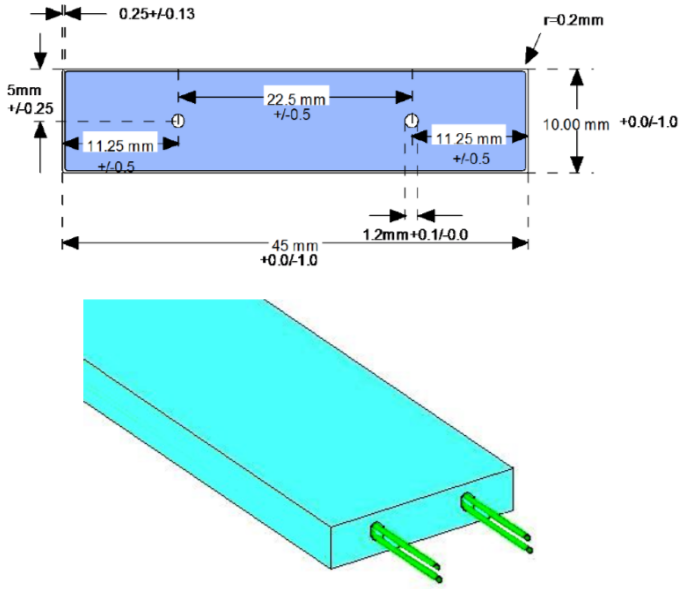


Figure 5: Top: Design dimensions of the scintillator cross section. Bottom: Rendering of the strip with two fibers in each hole.

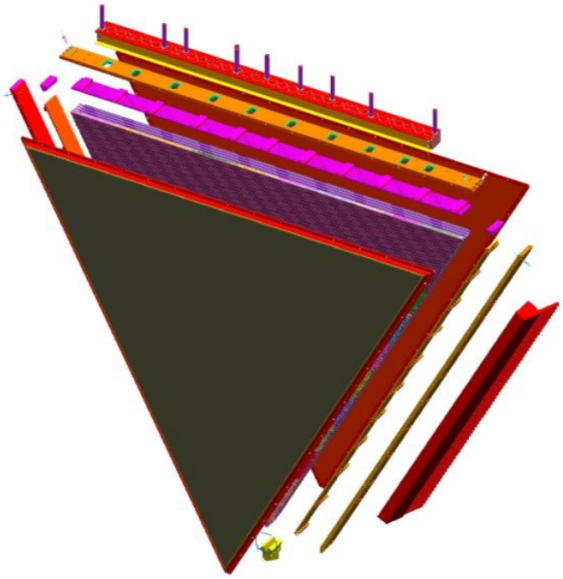

Figure 6: CAD model of one of the six PCAL module boxes showing the front/rear composite windows, side-wall supports, and lead/scintillator sandwich.

estimates, we concluded that the best choice for the PCAL components were: Fermilab (FNAL) extruded scintillator, the Kuraray Y11 multi-clad 1-mm-diameter WLS fiber, and the Hamamatsu R6095 PMT, selected to have quantum efficiency >16% at 500 nm. We also evaluated extruded scintillators from Amcrys-Plast/Kharkov (Ukraine), WLS fibers G91A from Bicron, and the Hamamatsu PMT R1450 (selected to have >18% quantum efficiency at 500 nm) but these did not meet the combined price and performance targets for PCAL.

### *4.1. Mechanical Support*

The PCAL box consists of two composite windows of 25.4 mm ROHACELL structural foam core (FR-3715 Last-A-Foam, density 0.24 g/cm$^3$) sandwiched between two 2 mm stainless steel sheets. Each window set is held together by a stainless steel "L" frame welded around the perimeter. The front and rear windows are bolted to three aluminum side-walls, which complete the structural members of the box (see Fig. 6). All lead and scintillator layers inside the box are held in position by a retaining assembly attached to two of the side-walls. These retainers also create a space between the side-wall and the end of the scintillator strips that is used, together with machined slots and channels, to route the light readout fibers out of the box to the PMT housings (see Fig. 7). At the PMT readout end, the fibers pass through the three holes of the black PVC adapters to which the PMT is mounted (see Fig. 8). There the fibers are glued into the adapter, then milled, polished (see Section 5.3), and coupled to the PMTs with optical grease. The opposite ends of the fibers extend from the far end of the strips by ~1 mm and are spot glued to the scintillator.

### *4.2. Scintillators*

The scintillator strips used in PCAL were manufactured at the FNAL-NICADD Extrusion Line Facility. The nominal dimensions were 500 mm × 45 mm × 10 mm. The polystyrene base of the scintillators was Dow STYRON 663 W. The primary dopant was 2,5-diphenyloxazole (PPO, 1% by weight). The secondary dopant was 1,4-bis (5-phenyloxazol- 2-yl) benzene (POPOP, 0.03% by weight). A reflective surface coating of polystyrene with 12% $TiO_2$ of 0.25 mm nominal thickness was co-extruded during the manufacturing process. Each strip has two holes through the length of the strip, which were also co-extruded. The holes were intended to allow easy insertion of two 1-mm-diameter fibers.

Scintillators from FNAL were delivered to Jefferson Laboratory (JLab) with two lengths: 420 cm (1450 strips used for U-views) and 450 cm (2710 strips used for V,W-views). Cutting of the strips was performed at JLab and at the College of William and Mary (WM). The average width for the scintillators to be used in a given layer was measured before the scintillators were cut, and the final cut length of each strip needed to fit within the triangular area was chosen based on this average to avoid buildup of errors during stacking. The largest deviation from the design width of 45 mm was less than 0.3 mm, compared to the specified tolerance for this dimension of ±1 mm. For each module the position accuracy from layer-to-layer was better than a few millimeters. The largest module-to-module variation in average width was 0.12 mm.

### *4.3. Wavelength Shifting Fibers*

Charged particles traversing the scintillator strips produce an emission spectrum ranging between 370-450 nm. The photons are down-converted and transported to the PMTs via the WLS fibers. An initial design for the fiber readout proposed using

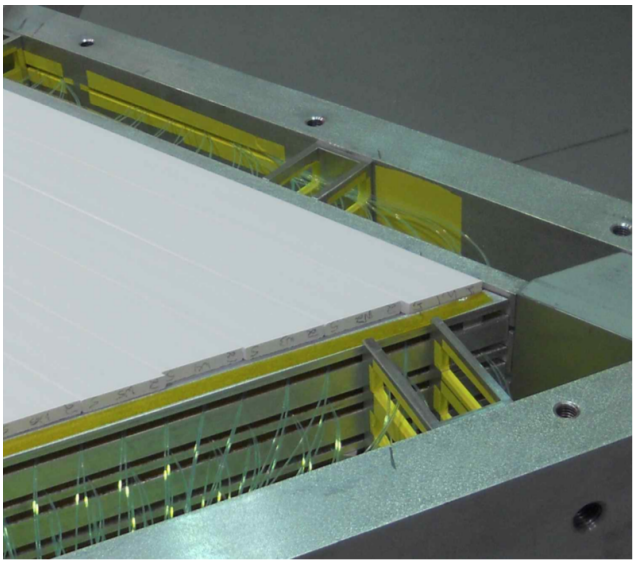

Figure 7: Retainer assembly at the corner of the VW and U readout sides of the PCAL box. Yellow mylar tape is applied at locations of potential abrasion of the WLS fibers.

three WLS green fibers embedded in straight grooves running the length of the scintillator surface, and the R&D studies discussed above [10] were based on prototypes of this configuration. A later study [11] showed that through-holes inside the scintillator would enhance the light yield, since the fiber would be fully enclosed. The question arose as to how the holes can be efficiently filled with epoxy for the large scintillator pieces to avoid air bubbles and pockets. Also it was important to characterize the light transmission characteristics of the scintillator with and without epoxy.

Finally, it was concluded [12] that while a gluing procedure could be developed with good reproducibility, careful and time consuming attention was required for large-scale production. These same studies also showed that two WLS fibers per hole without glue gives approximately the same transmission characteristics as a single fiber with glue (see Fig. 9). It was also found that less attenuation was produced without glued fibers. The added expense of the extra fiber was more than offset by a much faster and simpler assembly procedure together with a likely more uniform light collection efficiency.

### *4.4. Photomultiplier Tubes*

Assembly and testing of all 1200 of the Hamamatsu R6095 PMTs assigned to PCAL was performed at James Madison University (JMU). Figure 10 shows the individual elements of each PMT assembly. Each high voltage (HV) divider supplied with the PMT was tested for correct voltage at the output pins. The base assembly consisted of soldering HV, signal, and ground cables between the divider and connector terminals on the end cap. Spacers were cut and installed on either side of the spring to provide the desired compression force between the PMT and fiber adapter upon installation. DC dark current measurements were made at 1000 V for PMT acceptance testing and stored in a MYSQL database for later reference. The JMU dark current

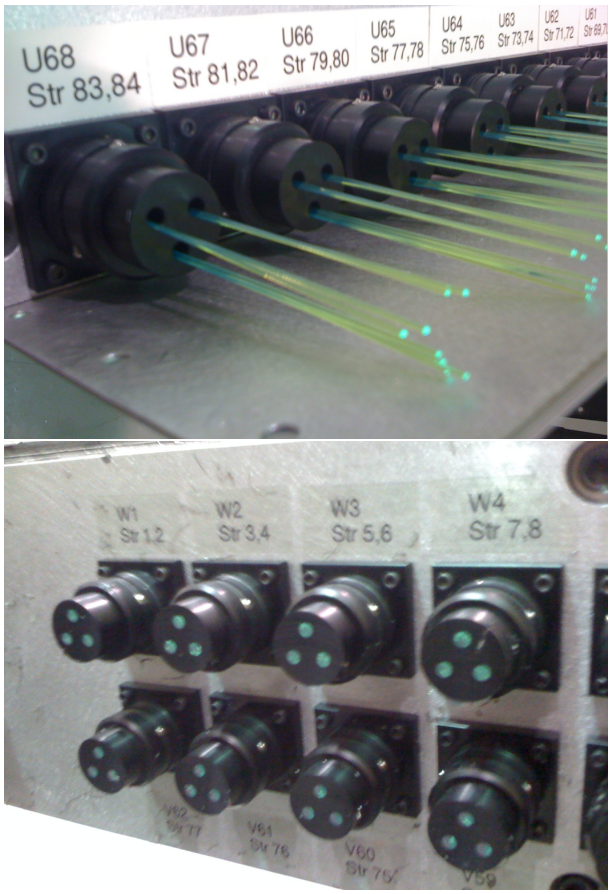


Figure 8: Top: WLS fibers from the scintillators extending from the PMT attachment mounts fixed to the PCAL bulkhead. Bottom: WLS fibers after gluing, milling, and polishing prior to PMT installation.

measurements showed a considerably smaller mean and variance compared to the test data from Hamamatsu as shown in Fig. 11.

### *4.5. Lead*

Between two scintillator layers, there is one lead layer. For each PCAL module, there are a total of 14 lead layers. Each layer consists of two right-angle triangle shaped sheets, where the hypotenuse of each triangle is parallel to the V or W sidewall. Thickness uniformity of each layer was checked using a CheckLine TI-25DL ultrasonic thickness gauge with 72 sample points measured per layer (36 for each half-layer). A droplet of coupling liquid between the transducer and lead was used to ensure reproducible sound transmission for each measurement. Distributions of these sample points from all 14 layers in each module is shown in Fig. 12.

## 5. Assembly and Installation

Construction and acceptance testing of each PCAL module was performed at JLab. Procedures included cleaning and assembly of the PCAL box, followed by stacking of the scintillator strips and lead sheets, routing of the WLS fibers and spot gluing at both ends, milling and polishing of the WLS fibers at

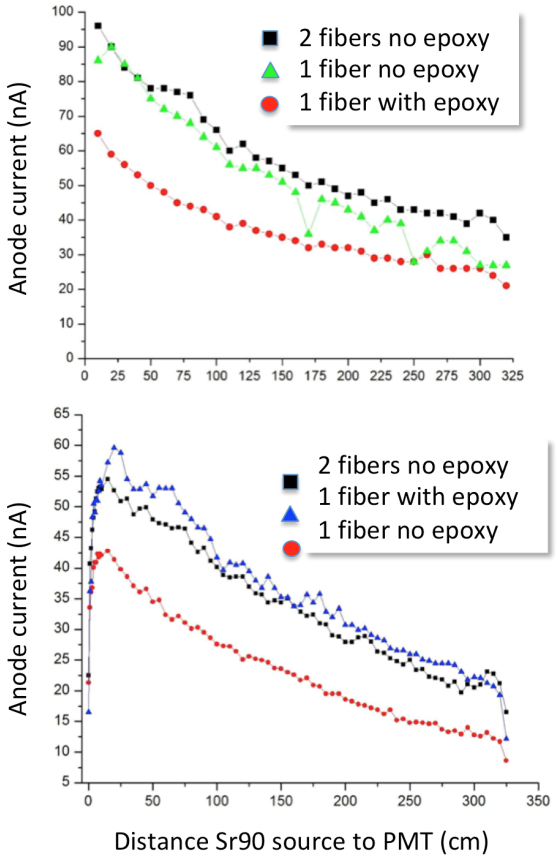


Figure 9: Relative light yield of various WLS readout fiber configurations. Top and bottom plots compare different gluing procedures for fibers secured in holes filled with epoxy.

the PMT readout adapter, and ending with final shimming and installation of the downstream composite window. Scintillator and fiber acceptance testing occurred in parallel in the same work area.

### 5.1. Scintillator and Fiber Testing

Prior to assembly of each PCAL module, acceptance testing of the transmission properties of the scintillator strips and WLS fibers was performed in a light-proof box using a computer-automated system. The apparatus used a PMT to measure the light output of the scintillator-fiber combination in response to a $^{90}$Sr beta source that was moved along the length of the scintillator strip. During scintillator testing, a set of four test fibers, glued to a plastic adapter in contact with the PMT photocathode, were inserted into the scintillator (two fibers per hole). The PMT anode current was measured using a Keithley multimeter with 500 samples taken at 10 cm intervals along the strip. Quality acceptance was based on the uniformity of the response and a typical exponential dependence on source position. Measurements were made for all of the longest (>200 cm) scintillator strips used in PCAL.

Studies at fixed distances of $x = 10$ cm and $x = 170$ cm showed light yield variations <5%, while transverse variations at $x = 10$ cm for four different source position were also


Figure 10: Photograph and schematic shows the housing assembly for the Hamamatsu R6095 1-in diameter PMT used in PCAL. The bulkhead mount fiber holder was outfitted with an O-Ring and three push-fit ball plungers to ensure a snug and light-tight push-on fit for the PMT housing.

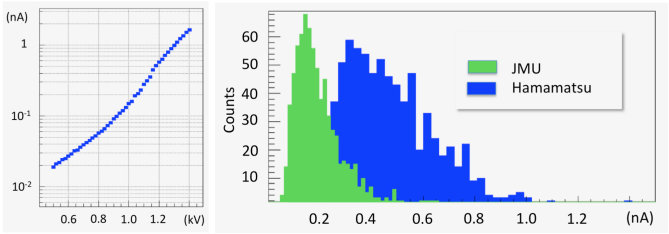


Figure 11: Left: Typical measurement of anode dark current vs. voltage for the Hamamatsu R6095 PMTs used in PCAL. Acceptance testing was performed at 1000 V after a 30 minute warm-up time. Right: Distribution of PMT anode dark current measurements from JMU and from Hamamatsu. The JMU distribution mean is 0.2 nA.

<5%, indicating good uniformity of the scintillator batch and no strong transverse dependence of fiber light collection efficiency. More complete measurements of the light yield of the shortest and longest strips tested are shown in Fig. 13, where the position dependence $I(x)$ of the PMT current is shown fitted to a double exponential,

$$I(x) = A_S \exp(-x/\lambda_S) + A_L \exp(-x/\lambda_L). \quad (1)$$

From fitting a large sample of scintillators it was found the attenuation parameters were clustered around the average values $\lambda_S = 70$ cm and $\lambda_L = 400$ cm. By fixing these short and long attenuation factors at their nominal values and refitting, it was found that the stability of the fitted amplitudes was around 17% for $A_S$ and 5% for $A_L$ for the group of scintillators studied.

Testing of the WLS readout fibers was performed with the same apparatus, using a test scintillator 30 cm in length. Five

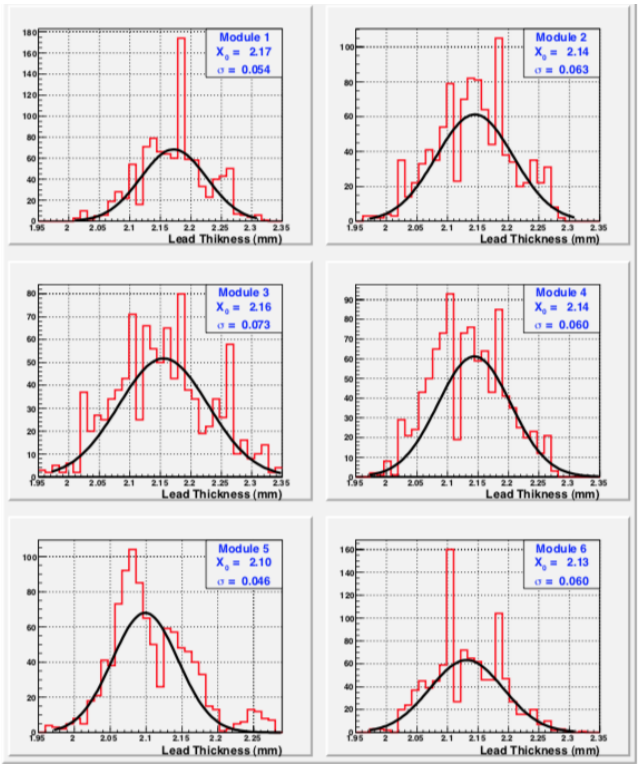


Figure 12: The distribution of measured thicknesses of the lead sheets for each of the six PCAL modules.

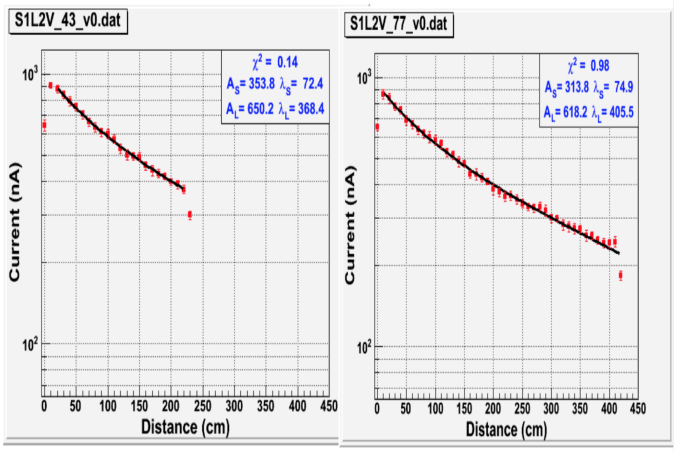


Figure 13: Measurements of the PMT anode current vs. $^{90}$Sr source position for a PCAL scintillator fitted with 4 WLS readout test fibers. Here a double exponential is fit to the shortest (left) and longest (right) strips studied.

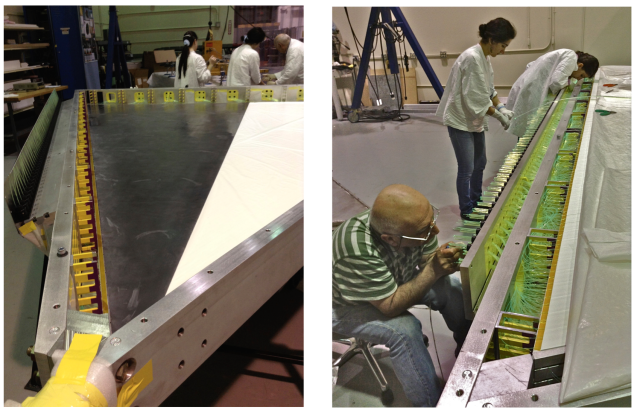

Figure 14: Left: Interior of a PCAL box during scintillator/lead stacking. A half layer of lead is shown in place. Right: WLS fiber routing and gluing operations.

sets of four fibers each were selected at random for testing from each packaged bundle of 100. A single measurement of the PMT current with and without fibers inserted was made by placing the $^{90}$Sr source at the midpoint of the scintillator. In all cases, fibers whose response was below the nominal measurement by >15% were found to have mechanical damage, although other fibers from the package were tested to double-check batch uniformity. Overall, the light yield stability of the fiber response was better than 7%.

### 5.2. *Lead-Scintillator Stacking*

Each PCAL box were cleaned with isopropanol to remove any grease and debris from machining. The bottom window was placed on a support table and the side-walls and retainers were installed. Prior to scintillator stacking, a 50 $\mu$m Teflon sheet was laid down, followed by placement of the first U layer of 84 scintillator strips, beginning with the longest strip. Gaps between the scintillators were minimized both during placement and after each layer was complete using shimmed triangle pieces in the corners to push the strips together. Strips were also tightly bound between the retainers at the fiber readout end and flat spring clips at the opposite end to accommodate any thermal expansion.

Once all the scintillator strips were in place for a given layer, four WLS readout fibers were inserted, one at a time, into the two holes for each strip. After scintillator insertion, each fiber was cut to a length that was predetermined to allow the fiber to reach the PMT adapter holes and extend beyond by about 3 cm. (see Fig. 14). This customized length was also designed to prevent sharp turns that fall below the minimum bend radius for these fibers for the particular routing needed. After fiber installation and routing for all scintillators in the layer was complete, continuity and correct placement of each fiber was checked using a blue LED at the far end of the strip and a photometer at the PMT base. The final step was to spot glue all fibers at the far end to the scintillator. This was done using Dymax optical UV curing adhesive OP-4-20632. Care was taken to leave an air hole to permit the flowing of dry nitrogen through the PCAL volume during its lifetime.

Lead sheets were stored on a pallet and positioned into the PCAL box using a movable gantry and a crane with fine position control. Suspended from the crane was a strongback with 12 vacuum-pumped suction cups to uniformly lift the sheet and place it precisely in position, making sure the edge of the scintillator matched the edge of the lead plate. Each lead layer was divided into two half-sheets to make installation more manageable (see Fig. 14). For each PCAL module a total of 14 lead sheets and 15 scintillator/WLS layers were installed.

### 5.3. WLS Fiber Cutting and Polishing

The milling and polishing operation was performed with a fiber bundle cutting device designed and built at YERPHI and previously used for the ATLAS tile calorimeter [13]. The machine was brought to JLab and re-commissioned to mount directly onto the PCAL U and V,W PMT side-walls, using a precisely aligned cutting-polishing head moving along a polished steel guide track. The cutting head had two sets of tungsten alloy knives for rough and fine cutting, with a round cut edge design in order to obtain a smooth surface during overlapping knife passes. The tool operated in a continuous motion, making several rough cut and milling passes (see Fig. 15) and ending with a single polishing pass. The cutting head could be operated either manually or automatically.

Figure 15: Fly cutter of fiber cutting machine making an initial milling pass of PCAL WLS fiber bundles.

### 5.4. Installation in Hall B

Each PCAL module was mounted on the CLAS12 Forward Carriage (FC) directly in front of the existing EC module, using an installation tool suspended from the overhead crane consisting of a strongback and a counterweight to offset the 8 ton PCAL weight (see Fig. 16). The PCAL nose was bolted to a central hub on the FC apex, while brackets on the V and W corners mounted to arms welded to the FC.

The output signals from the PCAL PMTs are routed to the FC with a single run of RG-58 coaxial cable. The EC PMT signals use RG-8 cable with RG-58 patch cables at both ends for a more flexible routing geometry. Both the EC and PCAL rely on passive resistive splitters designed and built at the University of Virginia to distribute the signals to digitization electronics located in VME/VXS crates. The split ratio is 2:1 for the PCAL and 3:1 for the EC. For both calorimeters the larger signal goes to the analog-to-digital (ADC) modules. Mapping of the patch cables from the splitter to the electronics follows the same sequential detector mapping used for the input to the splitters.


Figure 16: Left: Installation of PCAL module onto the Forward Carriage in Hall B at the Sector 5 position. U PMTs fit into the gap between the EC modules. Right: PCAL module installed in front of the existing Sector 5 EC module. The yellow lifting fixtures were later removed.

The VME/VMX crates and high voltage (HV) mainframes are installed in six groups of racks on three levels of the FC that are located behind each of six sectors containing the PCAL/EC/FTOF/LTCC modules (and RICH in Sector 4) (see Ref. [2] for details). The calorimeters use both CAEN 1527LC and 4527 HV mainframes outfitted with negative polarity 24-channel A1535N cards that fit into slots at the rear of each mainframe. The PCAL HV cards are housed in the same mainframes used by Forward Time-of-Flight (FTOF) system [14].

From the splitters, thin coax patch cables are routed to JLab VME-based Discriminator Scaler Module (DSC2) boards for pulse timing measurements and JLab 250 MHz 12-bit flash ADCs (FADC) for pulse amplitude measurements [15]. Ribbon cables connect the DSC2 with CAEN 1190A TDCs that have 100 ps LSB resolution. The FADC and DSC2/TDC modules are housed in separate VXS crates. The FADC/VXS crate also contains the JLab VXS Trigger Processor (VTP) in a special switched slot that is used to process the energy and hit data from the FADCs for the CLAS12 trigger decision making [15, 16].

All HV and RG-58 signal cables for the PCAL were manufactured at Ohio University. The thin coax interconnection cables were manufactured at Norfolk State University. Both groups also participated in cable installation in the test setup and on the Forward Carriage in Hall B.

### 5.5. Cosmic Tests

Initial evaluation of the PCAL performance was performed immediately after construction of each module using a test data acquisition (DAQ) system adjacent to the assembly area. PMT installation and cabling was followed by gradual application of HV and the use of raw discriminator scaler data to identify and

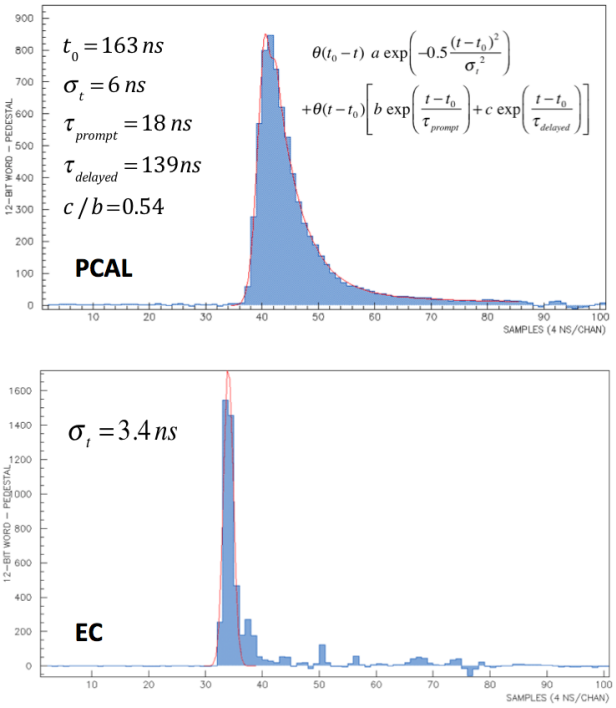


Figure 17: Comparison of pedestal-subtracted FADC waveforms for PMTs in the PCAL (top) and EC (bottom). Energy deposition resulted from cosmic triggers, where larger than typical amplitudes were selected to illustrate waveform shape. Fits to the PCAL shape used the expression shown, with typical fit parameters indicating the prompt and delayed components.

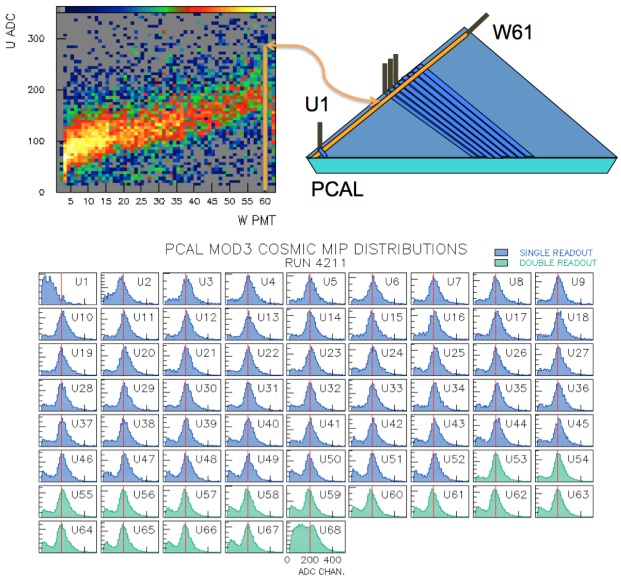


Figure 18: Top: Schematic showing the method used to perform PMT gain matching. The U strip PMTs use crossing W strips as a proxy for light readout distance, while a multiplicity cut $N_u = N_v = N_w = 1$ vetoes non-vertical muons. The left plot shows the attenuation of readout light in a U PMT from cosmic hits when plotted vs. W PMT strip number. All U PMT gains are adjusted to center the minimum-ionizing particle (MIP) ADC peak at channel 200, using W strip 61 to fix the readout distance at minimum attenuation. Bottom: Summary of MIP calibration for all U strips. Edge strips U1 and U68 show contributions from non-vertical muon trajectories that cannot be vetoed.

repair malfunctioning PMTs and sources of excessive noise. Repairs were dominated by breakdown noise requiring extra mylar film insulation, cold solder joints of ground braids within the HV dividers, and pinhole light leaks in the RTV silicone beads used to seal the external sheet metal housings.

Test procedures included using a cosmic muon trigger to establish digitization configuration parameters for the FADCs based on measurement of the PMT pulse waveforms. The trigger was based on an OR of all W PMTs from the DSC2 timing discriminators. The FADC parameters include the timing, relative to the trigger, of the pulse capture window, the number of samples in the window, and the threshold of noise suppression. An example of the PCAL PMT waveform for a 100 sample window aperture is shown in Fig. 17 (top), where each sample is 4 ns. Compared to the EC PMT waveform shown at the bottom of Fig. 17, which has a very short duration and rise time of 2-3 ns, the PCAL waveform leading edge has a 6 ns rise and a substantially extended duration, with both prompt and delayed components. The PCAL prompt response is likely due to the convolution of both the slower polystyrene ($t_{1/2} = 2-3$ ns) and Kuraray Y11 fiber ($t_{1/2} = 7-12$ ns) response times compared to the much faster BC-412 ($t_{1/2} = 1$ ns) scintillator used in the EC. Due to the delayed response, about 35 samples above threshold were necessary to capture 97% of the integrated PCAL waveform.

The location of the pulses within the window was offset to reserve the first 15-30 samples for mean pedestal measurements needed to provide a baseline for setting the readout threshold. The thresholds were set at 20 counts above the mean pedestal for cosmic calibration runs, and between 60 and 70 counts for CLAS12 production runs at high luminosity. Although the FADC modules contain configurable firmware to perform pulse processing, it was decided for initial CLAS12 running to take all FADC data without compression or firmware integration to enable offline analysis for optimization of pulse integration, timing, and background suppression.

The next step was to obtain an initial set of HV settings to gain match the PMTs. After a short period of PMT stabilization, each assembled module was calibrated using a loose cosmic trigger requiring hits in 2 out of 3 of the U,V,W views. The 1.2 kHz trigger rate was reduced by a factor of 20 using a software multiplicity cut to select near vertical muons before writing data to disk. This ensured a uniform minimum-ionizing particle (MIP) energy deposition of 10 MeV for the five scintillator layers viewed by each of the U,V and W PMTs (see Fig. 1). Events were selected close to the readout end to minimize light attenuation and the PMT HV settings were adjusted to normalize all MIP Landau distributions to the same ADC channel (see Fig. 18) using a power law relation between voltage and the desired relative gain change $\Delta V/V = (\Delta G/G)^{1/n}$. The value of the exponent $n$ needed to obtain rapid convergence was obtained with a few trial runs. Overall gain matching at the level of 3-5% was achieved.

These preliminary studies provided the starting point for more extensive calibrations in Hall B described in Section 7.

Also information on gain stability over the substantial storage time of some PCAL modules between construction and installation in Hall B was desirable, as well as on any systematic differences in the response to muons with PCAL in a horizontal test position compared to the vertical position on the Forward Carriage. Finally, studies of long-term changes in the light attenuation of the WLS fibers in PCAL will include these first measurements.

## 6. Cluster Reconstruction

Particles impacting the calorimeter produce localized energy depositions or *clusters*. Cluster reconstruction starts with the identification of *hits*, defined as scintillator strips having energy above a user-defined threshold, followed by the grouping of contiguous hits into one or more *peaks*. The criterion for a cluster requires the spatial intersection of three peaks, one from each of the U, V, and W stereo views. Each peak is represented geometrically as a three-dimensional line determined by the energy-weighted average of the mid-lines of each member strip. The schematic shown in Fig. 19 describes this geometric matching procedure. A more complete discussion can be found in Ref. [7].

Once the cluster is localized, the path from the cluster position to the PMT readout end is calculated for each U,V,W peakline and the peak energies are corrected for scintillator light attenuation. In addition, the peak timing is corrected for the propagation delay of the light, using the effective velocity of light determined for each scintillator from the calibration procedure. For isolated clusters the cluster energy is then defined as the sum of the corrected energy from each of the U, V, and W peaks that define the cluster. For multiple overlapping clusters, more sophisticated algorithms must be employed to correct the peak energy and timing data prior to cluster formation [7].

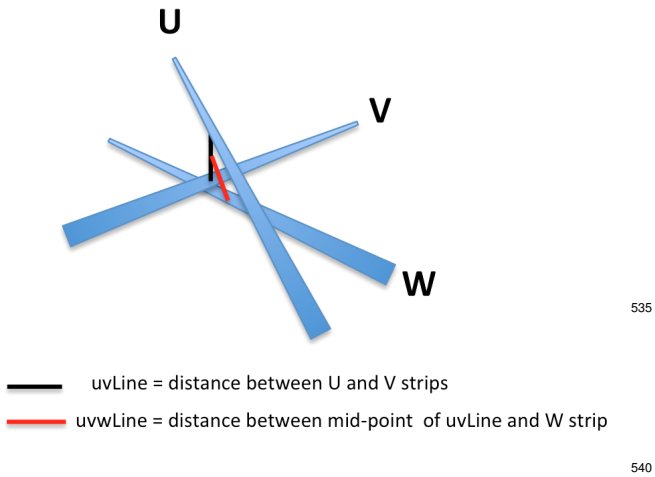


Figure 19: Schematic shows the 3D relationship of the U,V,W peaklines and the metrics used to define the cluster lab-frame coordinates $(x, y, z)$. A cut on the length of *uvwLine* defines the cluster, while the mid-point of *uvwLine* defines the cluster coordinates.

Each calorimeter module of ECAL is designed to measure only the transverse $(x', y')$ position of clusters in the local frame. In order to avoid parallax errors for tracks that are not normal to the face of the module, for PCAL the $z'$ reporting plane must be chosen to coincide with the layer of maximum energy deposition. Similar considerations apply to barrel calorimeters [17]. This effect is demonstrated in Fig. 20 using the CLAS12 Geant4 simulation package GEMC [18]. Here 2 GeV photons are generated diverging from the target position along the mid-plane and over the full polar angle $\theta$ range of PCAL. Using a $z'$ reporting plane at the first V strip (top) clearly introduces a $\theta$-dependent error in photon angle reconstruction, while moving this plane to the fourth V strip (bottom) minimizes this error. For the EC module the parallax shift is compensated by the projective geometry that was designed into the scintillators.

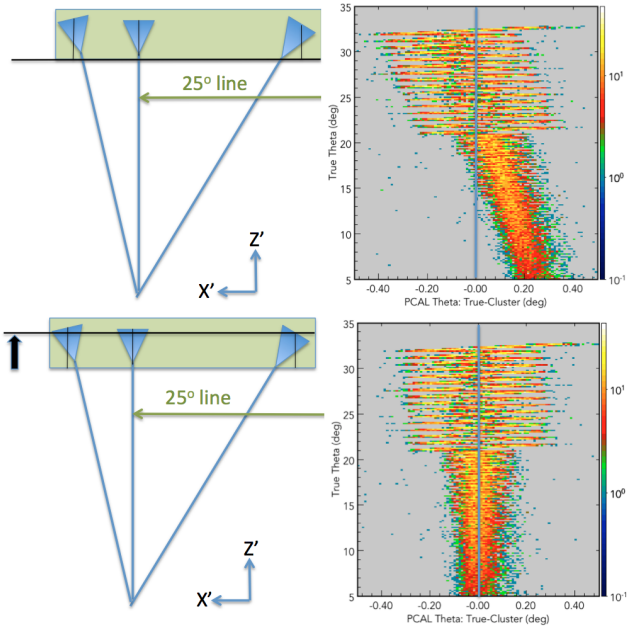


Figure 20: Left: Schematic shows how off-normal tracks with showers peaking at the rear of the calorimeter have a $x'$ projection at the front surface that creates parallax errors for a $z'$ reporting plane (black line) at the surface. Right: Geant4 simulation of 2 GeV photons originating at the target demonstrates the error in reconstructed $\theta$ for $z'$ at the first V strip (top) and the fourth V strip (bottom).

## 7. Calibration

Preliminary energy and timing calibrations of the ECAL were performed in preparation for the CLAS12 engineering and initial experimental physics runs in 2017-2018. Although the calibration algorithms were already honed from experience with CLAS, some additional complexity was introduced by the addition of the PCAL and the requirements of the FPGA-based physics triggers:

- Differences in the stereo readout geometry of the PCAL imposed the need to incorporate light attenuation corrections in the trigger firmware to ensure efficiency and spatial uniformity in the cluster energy reconstruction;
- Trigger efficiency studies and overall physics requirements required well-defined cluster energy thresholds for both electron and MIP triggers in each calorimeter layer (PCAL, ECIN, ECOU);

• Introduction of WLS fibers in the PCAL readout required more accurate time-walk corrections to compensate for the slower scintillator rise times in the PMT pulse.

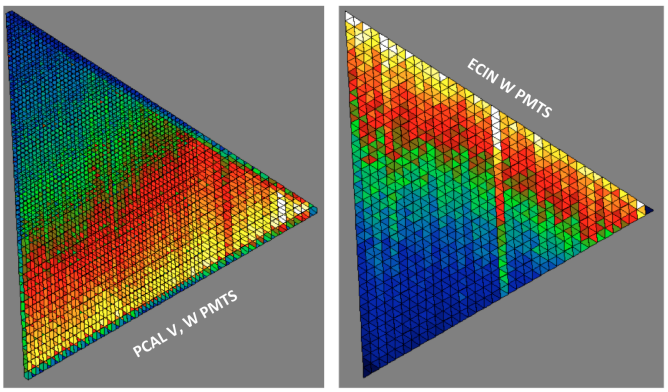


Figure 21: Pixel map of mean energy loss from MIP muons measured in Sector 5 W PMTs in PCAL (left) and ECIN (right). For each map the upper left corner is closest to the beamline. Note in PCAL both V and W strips are readout from the base of the triangle, while the ECIN W strips are readout along the right side. The color gradient from yellow to blue shows the light attenuation as a function of increasing distance from the readout end of each scintillator.

### 7.1. Energy Calibration

The longitudinal and transverse segmentation of the ECAL modules, together with the requirement for pattern recognition in the hodoscope design, means that cluster reconstruction from the full detector involves a minimum of 9 and up to 25 PMTs. The total detected energy $E_{det}$ results from the summation:

$$E_{det} = \sum_{m}^{3}\sum_{v}^{3}\sum_{n}^{N} E_n^{mv}, \quad (2)$$

$$E_n^{mv} = k(A_{sig} - A_{ped})/(a + ce^{-xb}), \quad (3)$$

$$E_{tot} = E_{det}/f_s, \quad (4)$$

where $E_n^{mv}$ is the measured energy in the $n^{th}$ PMT contributing to the peak in view $v$ and module $m$, and $k$ is a conversion from FADC units to MeV. The summation occurs over the $N$ PMTs in each peak, over the 3 U,V,W views for each module, and over the PCAL, ECIN, and ECOU modules. Here the terms *view* and *strip* always refers to the vertical grouping of scintillator strips whose light output is optically summed and measured by a single PMT. The measured quantities are $A_{sig}$, the integrated digitized PMT pulse from the FADC and $A_{ped}$, the FADC pedestal. The unknown quantities are the constants $a, b, c$ for the parameterization of the light attenuation as a function of the distance $x$ from the cluster to the readout end of the scintillator strip. For EM showers, the detected energy must be corrected by the sampling fraction $f_s$, to obtain the total deposited energy $E_{tot}$.

Since the energy of an electron incident on the ECAL is known from forward tracking, the energy calibration of the ECAL is in principle possible by adjusting the $a, b, c$ parameters and the sampling fraction $f_s$ until the reconstructed energy matches the known energy. However, compared to conventional readout geometries, the relationship in the ECAL between the total deposited energy $E_{tot}$ and the partial energies $E_n^{mv}$ is non-trivial for EM showers. A global optimization would require fitting hundreds of parameters per sector and might be very slow to converge.

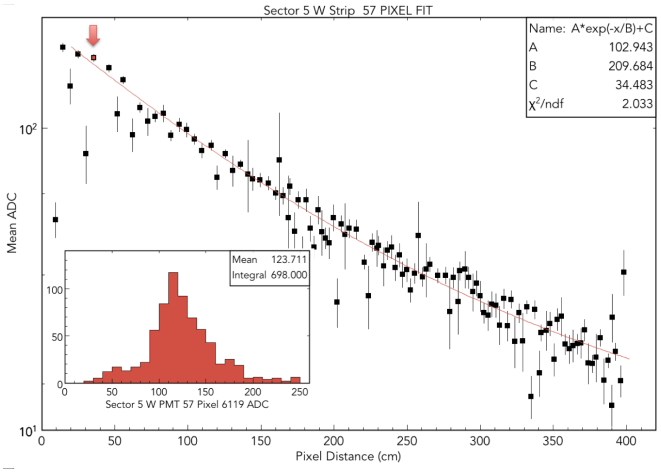


Figure 22: Typical fits to muon MIP mean energy loss as a function of PCAL pixel distance from the readout end of the strip. The inset shows the energy loss distribution in FADC units for the pixel highlighted by the arrow at top.

A simpler approach used successfully in CLAS with the EC and demonstrated with the PCAL in post-construction testing described in Section 5.5, is to proceed iteratively, using minimum-ionizing particles such as cosmic muons to simplify the energy deposition profile and to allow an independent determination of the $a, b, c$ parameters for each PMT. Then the PMT HV can be adjusted to produce a uniform overall response. Later, beam data taken with electrons and pions is used to estimate $f_s$ and to cross-check the MIP calibration. With the addition of PCAL to CLAS12 and the introduction of cluster reconstruction in the trigger, pre-calibration with cosmics is critical for evaluating the trigger performance of the ECAL.

Cosmic runs are performed using a special FPGA trigger that accepts only events where a single pixel has been activated. A pixel is the simplest possible cluster, and is the smallest unit of $x - y$ position resolution in the ECAL calorimeters, defined by the overlap of 3 scintillator strips, one from each of the U, V, and W views. Therefore a pixel must be visualized as a three-dimensional object. Requiring the muon to pass through a single pixel places the most restrictive cut possible on the particle track path length, thereby minimizing the spread in the MIP energy deposition.

A pixel map of the ECAL response to cosmic pixel triggers is shown in Fig. 21 for the W view strips in the PCAL (left) and ECIN (right). The color gradient in both plots clearly shows the attenuation of light as a function of readout distance from the pixel, as well as the overall variations in PMT gain near the readout end, such as the substantially brighter strip in ECIN W19. Also evident is the finer granularity of pixels in the PCAL compared to ECIN. Note that unlike the ECIN and ECOU modules, which have a constant pixel size, the PCAL pixels have a

variable size and shape due to the mixture of single and double readout strip widths and the different number of readout strips in U compared to V and W.

A typical attenuation response plot for a single PCAL PMT (W57) is shown in Fig. 22 from a cosmic run using a PCAL pixel trigger. The inset shows the energy loss distribution from a single pixel near the readout end of the scintillator stack and the mean of this distribution for each pixel are the points plotted in the main figure. The fit shown is used to obtain the $a, b, c$ calibration constants discussed above. Using this parameterization the muon MIP peak extrapolated to $x = 0$ is $a + c$. The desired FADC calibration for this peak corresponds to 10 MeV deposited energy in the 5-cm-thick scintillator stack (assuming $dE/dX(MIP) = 2$ MeV/cm). The PMT high voltages were iteratively adjusted until the peaks were matched within 5% of the desired calibration. These gains were then used for the initial round of data taking with an electron beam.

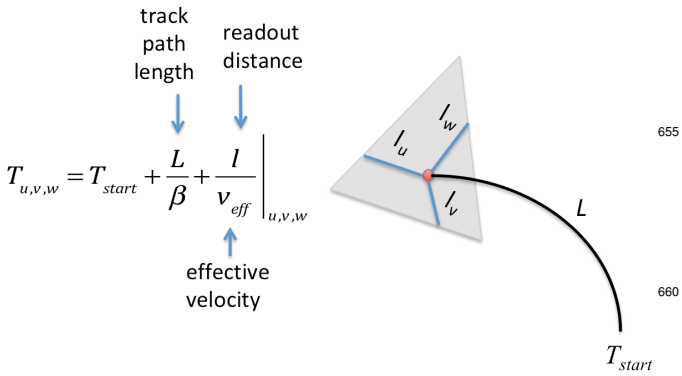


Figure 23: Cluster readout times $T_{u,v,w}$ at the edges of the calorimeter active area depend on the start time $T_{start}$, track path length $L$, and readout distances $l_{u,v,w}$. Particles with velocity $\beta \approx 1$ are chosen for calibration, while $v_{eff}$ is extracted from the fits to $T_{measured}$.

### 7.2. Timing Calibration

Optimal timing calibration in the ECAL is necessary both for neutral particle identification and background rejection. Identification of neutrons and photons from neutral clusters (those not matched with a charged particle track from the forward tracking) is based solely on time-of-flight from the target. The stereo readout and modular design of the ECAL provides considerable redundancy in the measurement of cluster timing, due to the multiplicity of PMTs that contribute to the total cluster energy. This allows flexibility in the choice of PMTs from which to construct the neutral event time. In addition, this redundancy can be crucial for rejecting accidental clusters formed from randomly overlapping background hits at high luminosity, especially when attempting reconstruction of neutrons.

The timing calibration of each PMT is based on analysis of clusters in the PCAL, ECIN, and ECOU arising from electrons, pions, and photons spanning a large range of position and deposited energy. A $\chi^2$ minimization is performed using six fitted parameters to adjust the difference between the measured time $T_{measured}$ (Eq. 5) and the expected readout time $T_{u,v,w}$ (see Fig. 23). These are defined, respectively, as:

$$T_{measured} = t_{TDC} + t_{ADC} \tag{5}$$

$$t_{TDC} = a_0 + a_1 \times TDC \tag{6}$$

$$t_{ADC} = \frac{a_2 + 300(100)}{ADC^{1/2}} + a_3 + \frac{a_4}{ADC^{1/4}}, \tag{7}$$

where the free parameters are the five $a_i$ coefficients and the light effective velocity $v_{eff}$.

Unit conversion of the raw TDC measurements and determination of the cable delays are absorbed into the $t_{TDC}$ term (Eq. 6). Corrections due to the amplitude dependence of the discriminated PMT pulse time are parameterized in $t_{ADC}$ (Eq. 7) using the integrated pulse from the FADC. Finally, the scintillator effective velocity $v_{eff}$ parameterized in $T_{u,v,w}$ is extracted from fits to $T_{measured}$. The $t_{TDC}$ and $t_{ADC}$ fits are performed alternately and iterated until convergence is reached. The $t_{TDC}$ fits are initialized with $a_2$, $a_3$, and $a_4$ in $t_{ADC}$ set to zero, using a fixed correction of 300(100) for PCAL(EC).

The procedure requires knowledge of the event start time $T_{start}$, the path length $L$ from the target vertex to the cluster position, together with the readout distances $l_{u,v,w}$ from the cluster as indicated in Fig. 23. These quantities are supplied by the various reconstruction services. Note that $T_{start}$ is synchronized to the RF pulse containing the incident electron and also compensates for the extended target vertex position.

For calibration purposes the cluster time is defined by the single PMT having the largest ADC value, in order to minimize the time-slew correction and maximize photon statistics. Typical uncertainties in the calibrated cluster time residuals are shown in Fig. 24 for the PCAL and ECIN U PMTs in Sector 1. The points show the means of the Gaussian fits to the residual distributions from each strip, where the mean variance is within 50 ps. The vertical red lines show the width ($\sigma$) of the fits, which represents the timing resolution averaged over all peak energies visible to that strip.

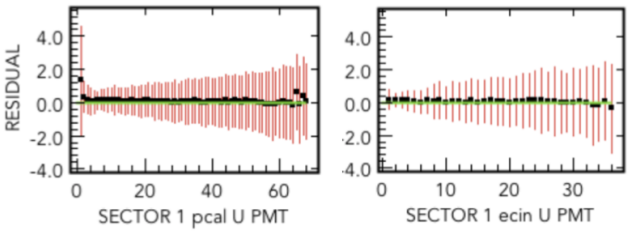


Figure 24: Residuals ($T_{measured} - T_{u,v,w}$) of calibrated cluster times in nanoseconds, plotted vs. U strip PMT number in the PCAL (left) and ECIN (right) calorimeters. The vertical red lines indicate the $\sigma$ of Gaussian fits to the residual distributions.

The deposited energy dependence of the timing resolution for typical strips in PCAL and ECIN is shown in Fig. 25, which clearly shows the improvement in resolution with increasing photon statistics. Although the PCAL has a 3-4 times larger

light yield compared to the EC, the broader time distribution of photons due to the WLS fiber conversion of the bulk scintillator light results in a somewhat worse resolution compared to the EC. Future development of the timing reconstruction will utilize both TDC- and FADC-derived timing from multiple PCAL and EC PMTs to determine the optimal contribution needed to provide the most accurate total energy cluster time.

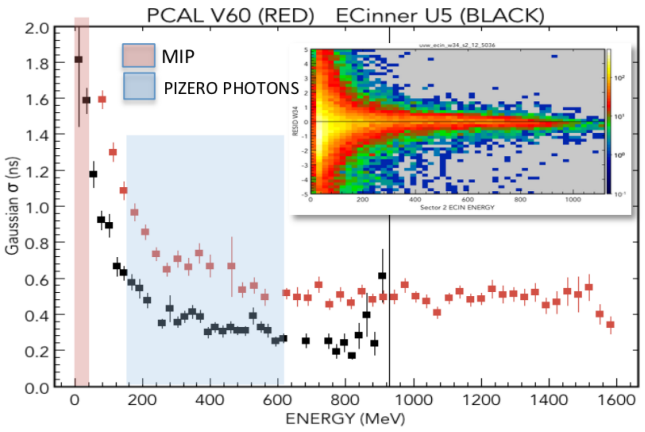


Figure 25: Deposited energy dependence of the timing resolution for typical strips in PCAL and ECIN. The red and blue bands show the energy ranges dominated by MIP pions and photons associated with $\pi^0 \rightarrow 2\gamma$ decays, respectively. The inset shows the 2D distribution of residual vs. energy for PCAL.

## 8. Performance

This section discusses preliminary performance of the ECAL using physics data production runs from fall 2018. This run period used beam energies of 10.6, 7.5, and 6.5 GeV with the CLAS12 torus magnet polarity set for both inbending and outbending electrons. The data presented here used the standard ECAL FPGA-based electron trigger [16] with a 15 kHz trigger rate and beam currents of 40 nA on a 5 cm $LH_2$ target.

### *8.1. Electron Response*

The response of the PCAL and EC components of a single ECAL module to high energy electrons is shown in Fig. 26. The beam energy was 10.6 GeV and outbending scattered electrons were selected by the Event Builder (EB) service [7] by matching a negatively charged forward track to ECAL clusters in the PCAL, ECIN, and ECOU and requiring an activated High Threshold Cherenkov Counter (HTCC) [19] mirror segment that matches the same track. The plot clearly shows the correlations between energy reconstructed in the front and rear sections of the ECAL, while the logarithmic $z$-scale emphasizes the range of fluctuations. The diagonal lines are the total reconstructed energy with the location of the total energy trigger threshold shown at PCAL+EC =300 MeV and the other line showing the maximum deposited energy consistent with the scattering angle cutoff at $\theta_{elec} = 6°$. Contributions from pions that exceed the 4.7 GeV threshold cutoff of the HTCC were rejected in the hardware trigger using a PCAL energy threshold of 60 MeV.

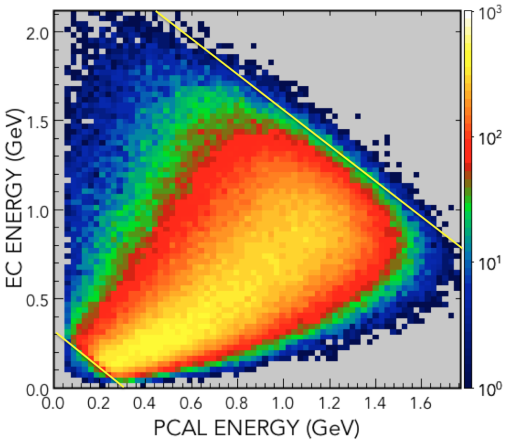


Figure 26: Reconstructed shower energy in the PCAL and EC modules in response to electrons with a momentum range of 1-10 GeV and a polar scattering angle range of 6°-34°. The energy is not corrected for the sampling fraction. The diagonal lines show the limits for the total reconstructed PCAL+EC energy.

The sampling fraction for electromagnetic showers is defined as the ratio of the total sampled energy (PCAL+EC) to the incident particle energy. The measured sampling fraction for electrons in the momentum range 1-10 GeV is shown in Fig. 27 as a function of the electron track momentum determined by the drift chambers [20] of the forward tracking system. The measurement is compared to GEMC simulations of electrons impacting the central portion of the ECAL, which show a dependence on the measured energy ranging from 0.22 to 0.255 over the range of electron momentum. The comparison shows there are a few percent systematic deviations due possibly to residual calibration errors.

The calorimeter energy resolution can be expanded as a function of energy with the usual parameterization of contributions [21]:

$$\left[\frac{\sigma(E)}{E}\right]^2 = \frac{\sigma_0^2}{E^2} + \frac{\sigma_1^2}{E} + \sigma_2^2 + \sigma_3^2 E \qquad (8)$$

- $\sigma_0$ - Pedestal noise, cross-talk;
- $\sigma_1$ - Poisson statistics (sampling, PMT);
- $\sigma_2$ - Calibration errors (PMT gains);
- $\sigma_3$ - Shower leakage fluctuations.

Typically $\sigma_0$ is ignored, although for MIP-based calibration analysis the contribution may be non-negligible. To minimize this contribution all CLAS12 PMT data are taken with FADC pedestals measured and subtracted event-by-event. Shower leakage contributions to $\sigma_3$ are most important for inbending electrons impacting the ECAL at the forward-most angles, where there is incomplete overlap of the PCAL and EC, and the CLAS12 acceptance vanishes. Leakage contributions are not expected to be significant for the outbending data considered here.

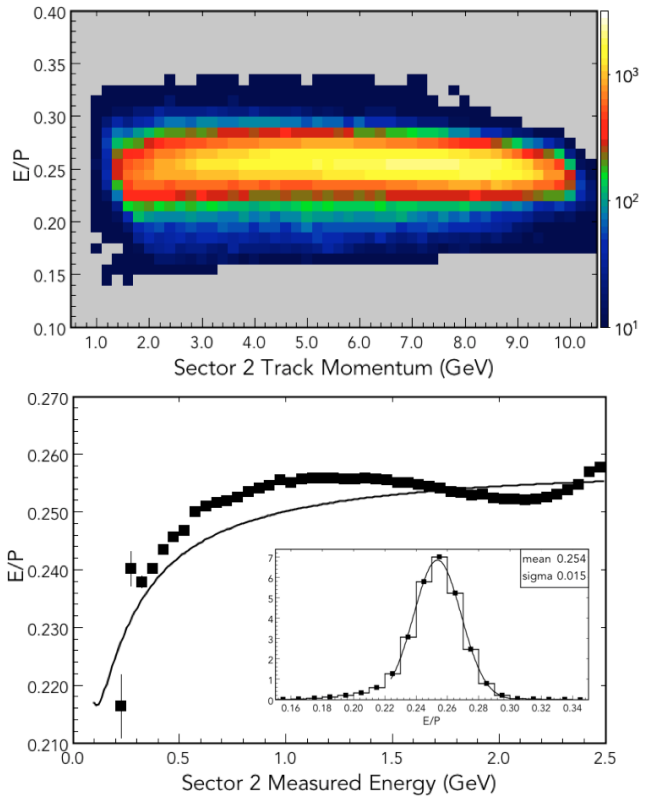


Figure 27: Top: Distribution of the ratio $E/p$ of the total reconstructed ECAL energy to the momentum of outbending forward tracks linked to clusters in the PCAL, ECIN, and ECOU that were identified as electrons by the Event Builder service. Bottom: $E/p$ vs. ECAL measured energy (black points) compared to the GEMC prediction (black line). The inset shows a Gaussian fit to the overall $E/p$ distribution.

Estimates of the contributions from $\sigma_1$ and $\sigma_2$ were performed using fits to the expected linear dependence of the total relative variance on the inverse of the electron energy as shown in Fig. 28. The summary of these fits shows an average energy resolution of $\sigma_1 = 0.09$ GeV$^{1/2}$, which is consistent with expectations from GEMC. The fit results for $\sigma_2$ of around 4% is typical of the present instabilities of PMT gain matching.

### 8.2. Position Resolution

The scintillator alignment and position resolution were estimated from comparison of the reconstructed position of shower clusters with the extrapolation of the forward tracking trajectory state vector of electron tracks from the target to the tracking planes of the PCAL and ECIN. Figure 29 summarizes the electron track-cluster matching residuals in the tilted local sector frame (with the $z$-axis normal to the ECAL face). Systematic offsets for the PCAL of ≈1 cm and ≈0.5 cm are seen in the radial (perpendicular to the U strips) and transverse (along the direction of the U strips) directions, respectively. These results are consistent with the present uncertainties in the absolute position of the calorimeter modules. The ECIN residuals have not changed from the CLAS era, although the fitted sigmas of the residual distributions are smaller, possibly due to the improved angular resolution of the CLAS12 forward tracking and smaller

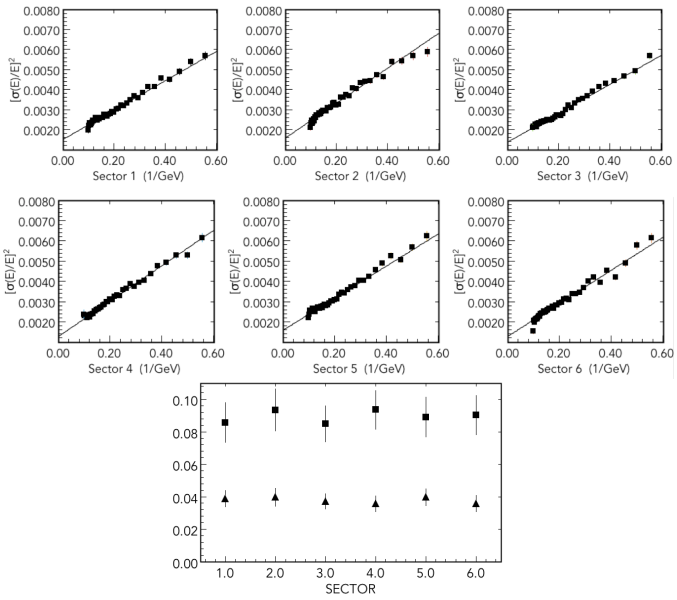


Figure 28: Relative variance of the measured sampling fraction plotted vs. the inverse electron energy. The linear fits used to obtain the resolution and calibration variance terms in Eq. 8 are summarized at the bottom, where $\sigma_1$(■) and $\sigma_2$(▲) are plotted vs. sector number.

multiple scattering at 10 GeV. The sector-to-sector variations in the residuals are much smaller than the offsets, and consistent with the estimated uncertainty in scintillator placement within each module. The sigmas of the PCAL residual fits imply an angular resolution of ≈1.2 mrad for showers in the CLAS12 Forward Detector. The measured offsets, together with survey data, will be used to further optimize the track matching cuts used for electron identification and background rejection.

### 8.3. Reconstruction of $\pi^0 \to \gamma\gamma$ Decays

Detection of the neutral $\pi$ meson requires reconstruction of the invariant mass $M$ of the $\pi^0 \to \gamma\gamma$ decay, using:

$$M^2 = 2E_1E_2(1 - \cos\theta_{12}), \tag{9}$$

where $E_1$ and $E_2$ are the energies of the two photon showers in the ECAL and $\theta_{12}$ is their opening angle. The $\pi^0$ energy can be determined from these same measurements in terms of the photon energy asymmetry $X$:

$$E_\pi^2 = \frac{m_\pi^2}{(1 - \cos\theta_{12})(1 - X^2)} \quad X = \frac{E_1 - E_2}{E_1 + E_2}. \tag{10}$$

Here $m_\pi$ corresponds to the physical $\pi^0$ mass of 134.98 MeV. The reaction kinematics following from Eqs. 9 and 10 are shown in Fig. 30. Clearly both the invariant mass and energy reconstruction are dominated by the ECAL angular resolution and accuracy at the highest energies, while at lower energies both the energy and angle resolutions contribute. Therefore this measurement can be used to reveal and refine the systematics and consistency of the energy calibration, geometrical alignment, and cluster reconstruction of the ECAL.

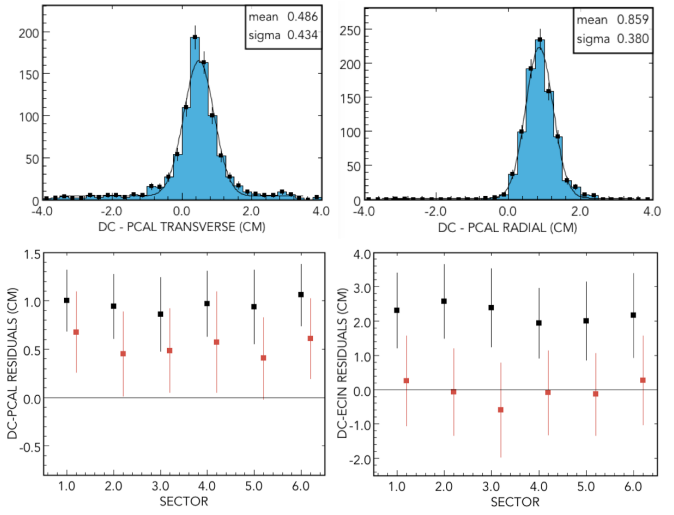


Figure 29: Top: Histograms show the distribution of residuals in Sector 3 between the projected hit position of forward tracks for electrons and the reconstructed PCAL cluster position for the radial (left) and transverse (right) coordinates. Bottom: Sector dependence of radial (black) and transverse (red) residuals for PCAL (left) and ECIN (right). The error bars show the sigma of Gaussian fits to the residual distributions.

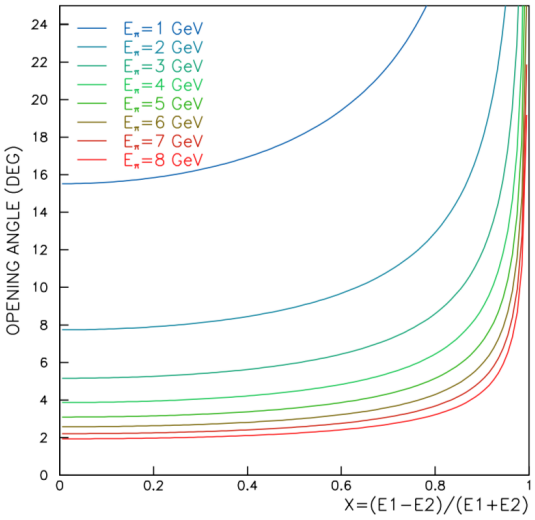


Figure 30: Opening angle of the $\pi^0 \to \gamma\gamma$ decay vs. the energy asymmetry $X$ of the two photons, shown for the range of $\pi^0$ energies measured in CLAS12.

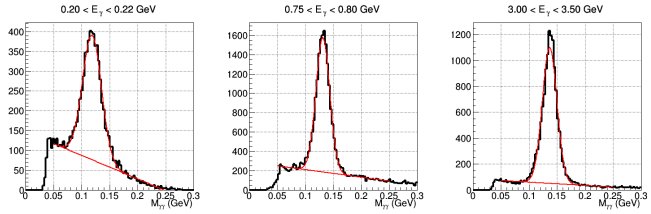


Figure 31: Empirical fits to both the combinatorial background and the invariant mass peaks reconstructed from two photons detected in the same sector of the ECAL. These data represent symmetric $\pi^0 \to \gamma\gamma$ decays where both photons are within the energy bins indicated in the plots. The fits shown are for photon energies of $E_\gamma$ = 0.21 (left), 0.77 (middle), and 3.25 GeV (right).

From Eq. 9 the following expression for the invariant mass resolution can be derived, expressed in terms of the uncertainties of the measured quantities:

$$\sigma_m = \frac{m_\pi}{2}\left[\left(\frac{\sigma(E_1)}{E_1}\right)^2 + \left(\frac{\sigma(E_2)}{E_2}\right)^2 + \sigma_{\theta_{12}}^2 \frac{\sin^2\theta_{12}}{(1-\cos\theta_{12})^2}\right]^{1/2} \quad (11)$$

For symmetric decays, where $E_1 \approx E_2$ or $X \sim 0$, it follows from Eq. 10 that the invariant mass resolution $\sigma_m$ reduces to a dependence solely on the pion energy $E_\pi$:

$$\sigma_m = \frac{m_\pi}{2}\left[\frac{4\sigma_1^2}{E_\pi} + 2\sigma_2^2 + \sigma_{\theta_{12}}^2\left(\frac{4E_\pi^2}{m_\pi^2} - 1\right)^2\right]^{1/2}. \quad (12)$$

From Eq. 12 it is possible to identify the contributions to $\sigma_m$ due to energy resolution $\sigma_1$, calibration error $\sigma_2$, and opening angle resolution $\sigma_{\theta_{12}}$ by measuring the invariant mass as a function of pion energy. This study was performed using a single 10.6 GeV run to accumulate a high-statistics sample of symmetric $\pi^0$ decays. Gaussian fits similar to those shown in Fig. 31 were used to extract the mean and sigma of the invariant mass peak over a photon energy range of 0.2-4.0 GeV, corresponding to a pion energy range of 0.5-8.0 GeV. Results from the fits are shown in Fig. 32, where a sector-based analysis (open symbols) and a global analysis summed over sectors (solid symbols) are plotted.

The analysis of symmetric decays, which are kinematically over-constrained, also permits an estimate for the photon energy correction [22], under the assumption that unphysical values of the invariant mass arise solely from this dependence. The GEMC prediction of the photon sampling fraction for the ECAL is shown by the solid line in Fig. 33. The calculated energy dependence and absolute magnitude depend largely on the lead-scintillator design and details of the inert material between the PCAL and EC and all pre-radiation in the materials in front of the ECAL. The fitted photon energy correction from the symmetric decay analysis is seen to follow the GEMC parameterization, with some systematic deviations that are being studied. Our current physics analysis uses the GEMC result.

### 8.4. Neutron Detection

Clusters in the ECAL not associated with any reconstructed forward track are designated neutrals by the Event Builder service [7]. Association of neutral PCAL clusters with ECIN and ECOU clusters are based on proximity to straight line trajectories from the target centerline to the PCAL cluster. Photons and neutrons are distinguished on the basis of the timing response, with neutrons defined as having velocity $\beta < 0.9$. Experiments that require the exclusive measurement of neutrons in the ECAL therefore demand both adequate timing resolution and sufficient detection efficiency.

Neutron reconstruction in the ECAL was studied using the $p(e, e'\pi^+)n$ reaction, with a cut on missing mass to provide a source of single tagged neutrons (see Fig. 34.) Data were taken with a 7.5 GeV beam energy. Events with missing momentum pointing into the fiducial region of the ECAL were selected.

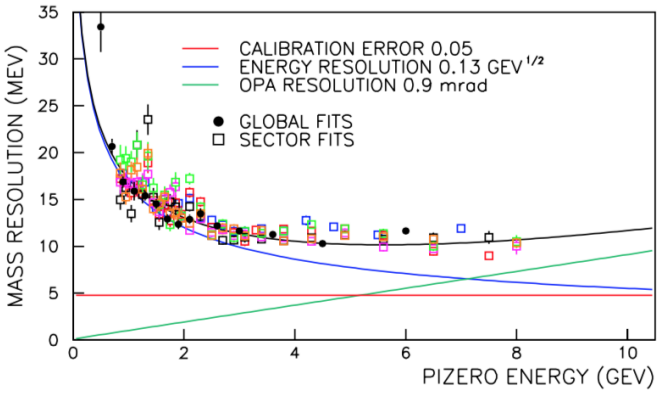


Figure 32: Summary of fits to distributions of invariant mass from $\pi^0 \rightarrow \gamma\gamma$ symmetric decays showing the mass resolution $\sigma_m$ vs. $\pi^0$ energy. A model of the mass resolution using Eq. 12 (black line) was fit to the energy dependence of $\sigma_m$ to extract estimates of the photon energy (blue) and opening angle (green) resolution, as well as the overall calibration uncertainty (red).

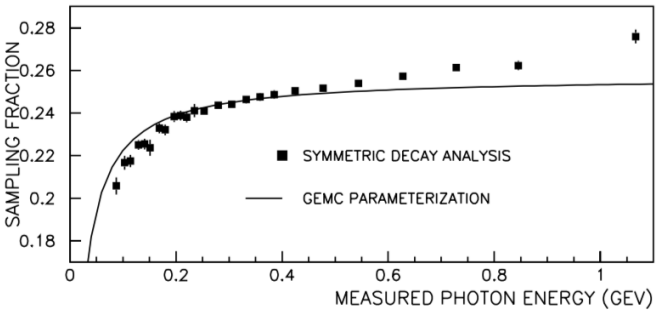


Figure 33: Summary of fits to invariant mass peaks from $\pi^0 \rightarrow \gamma\gamma$ symmetric decays used to determine the calorimeter sampling fraction for photons. The solid line shows the GEMC calculated photon sampling fraction.

Candidate neutron hits were identified by requiring the direction of the missing momentum to coincide with the direction of a measured neutral cluster within the expected angular resolution, assuming the target center as origin. Typical cuts used for these angular residuals are shown in Fig. 35 for the direction cosines $cx$ and $cy$ of the neutron momentum vector with respect to the beamline. Events that satisfy the angle cuts are plotted in Fig. 36. The data show a clear correlation between the measured velocity $\beta_{neutral}$ and the tagged-neutron momentum. The agreement with the expected correlation (black line) for a particle with the neutron mass indicates the timing calibration is reasonable. Some photon events are also visible, possibly from beam-related electromagnetic background from shielding structures. The resulting mass squared $M^2$ distribution calculated from the measured $\beta_{neutral}$ and missing momentum is shown in Fig. 37, where the photon and neutron peaks are clearly separated.

## 9. Summary

We have described the design, assembly, installation, and calibration of six new Pre-Shower Calorimeter (PCAL) modules

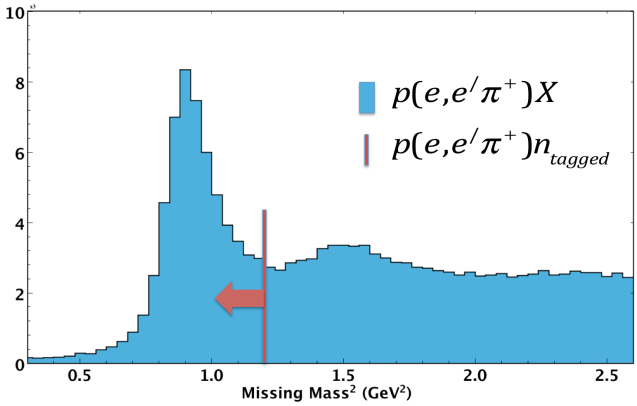


Figure 34: Missing mass $M_X$ distribution from detection of a $e'\pi^+$ final state using a proton target. The beam energy was 7.5 GeV. Single neutrons are selected with the cut $M_X^2 < 1.2$ GeV.

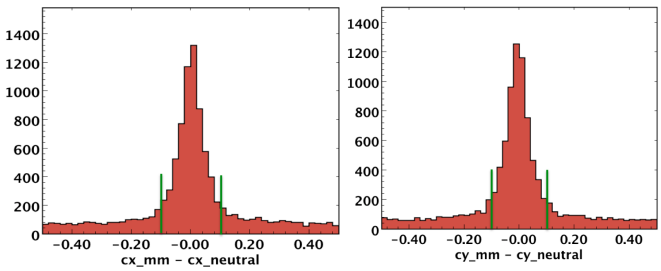


Figure 35: Differences in direction cosines between the missing momentum of the tagged neutron and the detected neutral cluster in the ECAL. The vertical lines show the cuts used to minimize the background from uncorrelated photons.

for CLAS12. The PCAL modules were built to extend the performance of the CLAS Electromagnetic Calorimeters (EC) for operation using beam energies up to 12 GeV. Both the PCAL and EC are sampling calorimeters that utilize a novel triangular hodoscope geometry with a combination of stereo transverse and threefold longitudinal readout of electromagnetic showers. The PCAL design extends the performance of the EC by increasing the total radiation length need to fully absorb electron and photon showers. In addition, the PCAL uses wavelength-shifting fiber readout to improve both the absolute scintillator light yield and the light attenuation, while the increase in transverse segmentation improves the spatial resolution by at least a factor of 2. Preliminary analysis of physics runs with 7.5 and 10.6 GeV electron beams indicate that the combined system of PCAL+EC meets the design goals for position, energy, and timing resolution, as well as electron trigger efficiency. At present we are still in the early stages of studying the luminosity and missing mass resolution dependence of the neutron and photon detection efficiency.

## Acknowledgments

Thanks to F.-X. Girod for the use of his preliminary analysis of $\pi^0$ energy corrections. Acknowledgments go to the Hall B engineering and technical staff for their careful attention to the

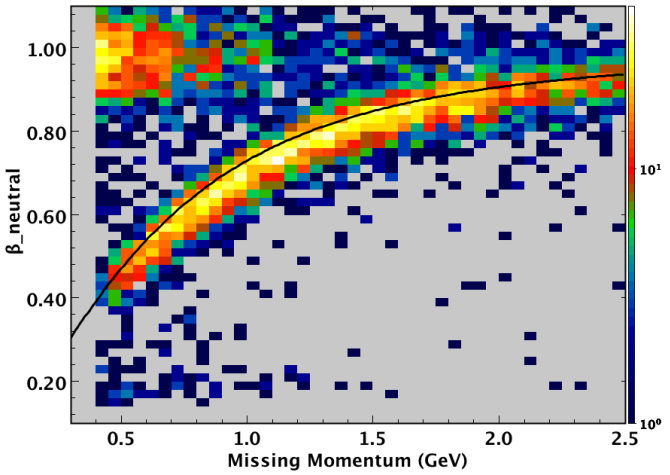


Figure 36: Correlation between the measured velocity $\beta_{neutral}$ of neutral clusters in the ECAL and the missing momentum of the tagged neutrals subject to the $\Delta cx, \Delta cy$ cuts shown in Fig. 35. The black line shows the expected correlation for neutrons.

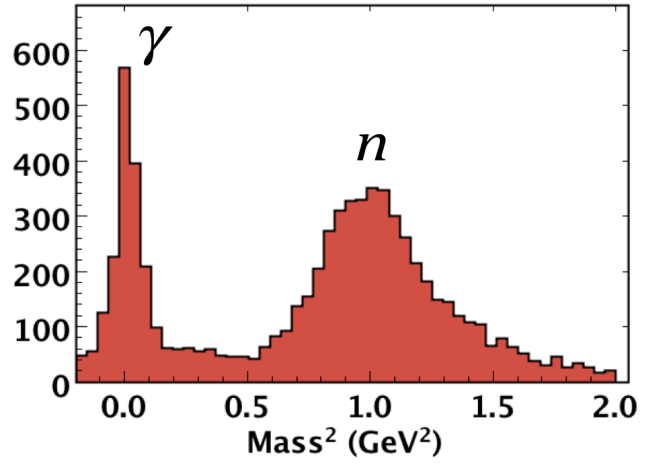


Figure 37: Mass squared distribution of neutrals detected in the PCAL and EC calculated from the measured $\beta_{neutral}$ and the missing momentum of the tagged-spectator neutrals. Both photon and neutron peaks are visible.

design, transportation, and installation of the PCAL modules. This material is based upon work supported by the U.S. Department of Energy, Office of Nuclear Physics Division, under contract No. DE-AC05-06OR23177 and was also supported by the National Science Foundation Major Research Instrumentation Project (MRI) grant PHY-0821173.

## References

[1] V. D. Burkert, Jefferson Lab at 12 GeV: The Science Program, Ann. Rev. Nucl. Part. Sci. 68 68 (2018) 405.

[2] V. D. Burkert, et al., The CLAS12 Spectrometer at Jefferson Laboratory, to be published in Nucl. Inst. and Meth. A, (2020) (see this issue).

[3] M. Amarian, et al., The CLAS Forward Electromagnetic Calorimeter, Nuclear Instruments and Methods Research A 460 (2001) 239–265.

[4] A. Rizzo, The meson spectroscopy program with CLAS12 at Jefferson Laboratory, http://inspirehep.net/record/1471392/ (2016).

[5] R. Minehart, et al., Lead-Scintillator Electromagnetic Calorimeter With Stereo Readout, CLAS-Note 90-014 (1990).
URL https://www.jlab.org/Hall-B/notes/clas_notes90/note90-014.pdf

[6] N. Dashyan, S. Stepanyan, Geant Simulations of the CLAS12 Pre-shower Calorimeter, CLAS-Note 2007-001 (2007).
URL https://misportal.jlab.org/ul/Physics/Hall-B/clas/viewFile.cfm/2007-001.pdf?documentId=346

[7] V. Ziegler, et al., The CLAS12 Reconstruction Framework and Event Reconstruction, to be published in Nucl. Inst. and Meth. A, (2020) (see this issue).

[8] G. Asryan, et al., The Geometry of the CLAS12 Pre-shower Calorimeter, CLAS-Note 2015-002 (2015).
URL https://misportal.jlab.org/mis/physics/clas12/viewFile.cfm/2015-002.pdf?documentId=18

[9] K. Whitlow, N. Dashyan, S. Stepanyan, The CLAS12 Pre-shower Performance Studies, CLAS-Note 2007-002 (2007).
URL https://misportal.jlab.org/ul/Physics/Hall-B/clas/viewFile.cfm/2007-002.pdf?documentId=348

[10] G. Asryan, H. Voskanyan, S. Stepanyan, CLAS12 Pre-shower Readout System, CLAS-Note 2007-007 (2007).
URL https://misportal.jlab.org/ul/Physics/Hall-B/clas/viewFile.cfm/2007-007.pdf?documentId=390

[11] D. Keller, M. Yurov, K. Hicks, S. Stepanyan, Scintillator Testing for Use in the Pre-shower Calorimeter, CLAS-Note 2009-008 (2009).
URL https://misportal.jlab.org/ul/Physics/Hall-B/clas/viewFile.cfm/2009-018.pdf?documentId=546

[12] A. Daniel, J. Riso, S. Stepanyan, W. Tang, H. Voskanyan, Light Transmission Characteristics of Scintillators for the Pre-shower Calorimeter, CLAS-Note 2010-012 (2010).
URL https://misportal.jlab.org/ul/Physics/Hall-B/clas/viewFile.cfm/2010-012.pdf?documentId=602

[13] F. Adamian, et al., Cutting-polishing device for TILECAL WLS fiber bundles processing, ATLAS Iinternal Note TILECAL-NO-1 (1997).
URL https://cdsweb.cern.ch/record/683591/files/tilecal-97-126.pdf

[14] D. S. Carman, et al., The CLAS12 Forward Time-of-Flight System, to be published in Nucl. Inst. and Meth. A, (2020) (see this issue).

[15] S. Boyarinov, et al., The CLAS12 Data Acquistion System, to be published in Nucl. Inst. and Meth. A, (2020) (see this issue).

[16] B. Raydo, et al., The CLAS12 Trigger System, to be published in Nucl. Inst. and Meth. A, (2020) (see this issue).

[17] T. D. Beattie, et al., Construction and Performance of the Barrel Electromagnetic Calorimeter for the GlueX Experiment, Nuclear Instruments and Methods Researh A 896 (2018) 24–42. doi:10.1016.

[18] M. Ungaro, et al., The CLAS12 Geant4 Simulation, to be published in Nucl. Inst. and Meth. A, (2020) (see this issue).

[19] Y. G. Sharabian, et al., The CLAS12 High Threshold Cherenkov Counter, to be published in Nucl. Inst. and Meth. A, (2020) (see this issue).

[20] M. D. Mestayer, et al., The CLAS12 Drift Chamber System, to be published in Nucl. Inst. and Meth. A, (2020) (see this issue).

[21] H. Gordon, R. Palmer, S. Smith, New Ideas in Calorimetry, Physica Scripta 23 (1981) 564–568.

[22] R. D. Masi, J. Ball, M. Garcon, F. X. Girod, F. Sabatie, Photon Energy Corrections in EC (from data), CLAS-Note 2006-015 (2006).
URL https://misportal.jlab.org/ul/Physics/Hall-B/clas/viewFile.cfm/2006-015.pdf?documentId=290